RSC Applied Interfaces

ROYAL SOCIETY OF CHEMISTRY

PAPER

View Article Online
View Journal

Cite this: DOI: 10.1039/d6lf00054a

Buried interfacial structures in cellulose-reinforced styrene–butadiene rubber composites probed by sum-frequency generation spectroscopy

Tatsuki Abe, *[a] Ryosuke Ozawa,[b] Tomofumi Maekawa,[b] Yuta Tsuji, [c] Satoru Yamamoto [a] and Keiji Tanaka *[ad]

Received 26th February 2026,
Accepted 3rd May 2026

DOI: 10.1039/d6lf00054a

rsc.li/RSCApplInter

The mechanical properties of polymer composites are closely linked to the aggregation states of polymer chains at filler interfaces. Here, we employed sum-frequency generation (SFG) vibrational spectroscopy to investigate the interfacial organization in styrene-butadiene rubber (SBR) composites reinforced with cellulose nanofibers (CNF). Phenyl groups from the styrene (St) units in SBR were found to adopt an oriented conformation at the buried SBR/CNF interfaces. Moreover, increasing the St content enhanced interfacial interactions, leading to improved dispersion of CNF within the SBR matrix. Molecular dynamics simulations were conducted to support the experimental observations and revealed that the local orientation of phenyl groups remained similar across compositions, while differences in CNF dispersion were attributable to interfacial energy matching. These findings provide molecular-level insights into structure–property relationships in polymer composites and offer guiding principles for the rational design of high-performance composite materials.

1. Introduction

Polymer composites, comprising a polymer matrix and fillers, have been widely used in tires and structural materials for transportation applications, including land vehicles and aircraft. The physical properties of polymer materials are markedly improved by the addition of fillers such as carbon black, silica particles, glass fibers, and modern nanocarbon materials.[1–3] The mechanism behind this reinforcement has been studied for over half a century to develop polymer composites with superior mechanical properties. One of the key factors in understanding the mechanical reinforcement of polymers is the adsorption of polymer chains onto filler surfaces, forming what is known as bound rubber, which cannot be removed even after leaching with good solvents.[4–6]

The thermal molecular motion of bound rubber has been extensively studied using techniques such as ^{1}H nuclear magnetic resonance,[5–8] dielectric relaxation spectroscopy,[9–12] and viscoelastic measurements.[13–16] These studies have revealed that the dynamics of bound rubber are markedly restricted compared to those in the corresponding bulk phase. Such restriction in mobility is thought to contribute to reinforcement through two principal models: one proposes that bound rubber forms a continuous, percolating network across adjacent fillers, efficiently transmitting applied stress,[17–20] while another suggests that filler particles aggregate to minimize interfacial free energy, independently forming a stress-bearing network.[21–24] Despite the contrasting mechanisms, both models underscore the importance of polymer chain behavior at solid–filler interfaces.

To gain molecular-level insight into such interfacial phenomena, numerous studies have employed model planar interfaces, enabling the use of techniques such as X-ray and neutron reflectivity measurements,[25–27] fluorescence spectroscopy,[28–30] and sum-frequency generation (SFG) vibrational spectroscopy.[30–32] These studies consistently show that segmental mobility is markedly suppressed near solid surfaces, and this suppression becomes more pronounced closer to the interface. SFG vibrational spectroscopy, which selectively probes non-centrosymmetric environments such as surfaces and interfaces,[33–42] has been widely used for interfacial analysis, although its application has largely been limited to idealized planar model systems due to experimental constraints. This limitation hampers direct

[a] Centre for Polymer Interface and Molecular Adhesion Science, Kyushu University, Fukuoka 819-0395, Japan. E-mail: t-abe@cstf.kyushu-u.ac.jp, k-tanaka@cstf.kyushu-u.ac.jp
[b] Sustainable Polymers Laboratory, Asahi Kasei Corporation, Kanagawa 210-0863, Japan
[c] Faculty of Engineering Sciences, Kyushu University, Kasuga 816-8580, Japan
[d] Department of Applied Chemistry, Kyushu University, Fukueoka 819-0395, Japan

observation of interfaces in real-world materials, where surface curvature and roughness differ substantially from model geometries. To bridge this gap, we have previously demonstrated the applicability of SFG spectroscopy to buried crystal/amorphous interfaces within semi-crystalline polymer films, leveraging the local breaking of inversion symmetry.[43–45] Building upon this foundation, our current work extends SFG analysis to more complex, buried interfaces within polymer composites, thereby enabling direct characterization of the local conformation of polymer chains in practical composite systems.

Recently, cellulose nanofibers (CNFs) have attracted much attention as fillers, serving as an alternative to inorganic fillers due to their lighter weight, superior mechanical properties, and low thermal expansion coefficient.[46–51] From a sustainability perspective, CNFs offer considerable advantages: they are derived from renewable biomass, their production is carbon neutral, and they exhibit minimal degradation during recycling. Despite these advantages, several challenges remain for the practical application of CNFs as fillers. For example, CNFs have multiple hydroxyl groups in their repeating units, making them prone to aggregation and resulting in poor interfacial adhesion with polymer matrices. Consequently, understanding and controlling the interfacial aggregation and conformation of polymer chains near CNF surfaces at the molecular scale is critical for optimizing composite performance.

In this study, we focus on styrene-butadiene rubber (SBR), a random copolymer of styrene and butadiene units that serves as a key elastomer in automobile tire applications, and investigate the interfacial conformation of SBR chains at CNF filler surfaces using SFG vibrational spectroscopy. Although CNF-reinforced elastomers have attracted interest, a molecular-scale insight into the polymer/filler interface remains limited. In particular, the influence of St content on interfacial polymer organization has not been systematically explored. Controlling the St content is expected to influence not only the interfacial aggregation states between the polymers and fillers, but also the mechanical properties of the resulting composites. However, because it also alters the intrinsic properties of the SBR matrix, the present study focuses primarily on the interfacial aggregation states rather than on the mechanical properties. To address this, we first identified the buried interface contributing to the SFG response, and then examined how varying the St content in SBR affects its interfacial structure with CNF. To provide molecular-level interpretation of the experimental results, we conducted atomistic molecular dynamics (MD) simulations, with a particular focus on the interfacial behavior of SBR chains at CNF surfaces.

2. Experimental

SBRs with styrene (St) contents of 6 mol% (SBR6), 12 mol% (SBR12), and 25 mol% (SBR25) were synthesized by anionic polymerization, also known as solution polymerization, and used as matrix polymers. The SBR chains contained both 1,2- and 1,4-addition polybutadiene units, referred to as 1,2-Bd and 1,4-Bd, respectively. CNF made from cotton linter was used as the filler. Characteristics of the SBRs, including number-average molecular weight (M_n), polydispersity index (M_w/M_n), glass transition temperature (T_g), and the ratios of St and 1,2-Bd, are summarized in Table 1. Fig. 1 shows the chemical structures of (a) SBR and (b) CNF.

Sheets of SBR6, SBR12, and SBR25 containing 7.14 wt% fillers, consisting of 5 wt% CNF and 2.14 wt% of a nonionic surfactant, were prepared by kneading and mixing each SBR with CNF. The thicknesses of the SBR6/CNF, SBR12/CNF, and SBR25/CNF sheets were 3.40 ± 0.15 mm, 2.95 ± 0.03 mm, and 3.12 ± 0.08 mm, respectively. For SFG measurements, all films were placed on quartz substrates. As reference samples, neat SBR films without CNF were prepared using the solvent-casting method with tetrahydrofuran (THF) solutions. These films were subsequently dried under vacuum for 24 h, resulting in thicknesses of approximately 5 μm. To clarify the origin of the SFG signals, SBR films containing 1 wt% CNF were also prepared on quartz substrates using the solvent-casting method. The resulting SBR6/CNF, SBR12/CNF, and SBR25/CNF films, with thicknesses of approximately 19, 32, 25 μm, respectively, were then dried under vacuum at room temperature (above T_g) for 12 h to remove residual THF.

The aggregation states of SBR at the interface with CNF in the composites were examined using SFG spectroscopy, a technique that provides superior depth resolution compared to other available methods. SFG measurements were taken using an SFG spectrometer (EKSPLA, Vilnius, Lithuania). A visible (VIS) beam with a wavelength of 532 nm was generated by frequency-doubling the fundamental output pulses of a picosecond Nd:YAG laser (PL2231-50, EKSPLA). A tunable infrared (IR) beam was obtained from optical parametric generation/amplification and difference frequency generation using BBO and $AgGaS_2$ crystals (PG500, EKSPLA). The incidence angles for the VIS and IR beams were set to 60° and 55°, respectively, with an ssp polarization combination (SFG:s, VIS:s, IR:p). The SFG signals were detected using a photomultiplier tube (PMT) (R7899, EKSPLA) after passing through a monochromator. X-ray computed tomography (CT) analysis was also performed on the SBR/CNF kneaded sheets to evaluate CNF filler dispersity, using a Skyscan-1272 system (Bruker, Billerica, MA, USA) with a rotation step of 0.2° per scan. The X-ray source voltage and current were set to 40 kV and 100 μA, respectively. Each image was accumulated four times. The pixel size of the detector was 1.2 μm square, and each image consists of 2452 × 1640 pixels.

MD simulations were conducted to better understand the aggregation states of SBR at the CNF interface using the Forcite module of Materials Studio 2024 software package (Dassault Systèmes, Vélizy-Villacoublay, France) with the COMPASSIII force field. A CNF surface structure was constructed based on the crystal structure of cellulose,[52] comprising two cellulose layers with dimensions of 8.0 × 8.3

Table 1 Characteristics of the SBRs

Samples	M_n	M_w/M_n	T_g/K	St ratio/mol%	1,2-Bd ratio in Bd/mol%
SBR6	127 k	1.12	215	5.8	40.3
SBR12	138 k	1.14	228	11.7	42.1
SBR25	158 k	1.11	249	24.5	39.3

nm^2. Random copolymer chains corresponding to SBR6, SBR12, and SBR25 were generated, consisting of St and Bd units in ratios of 6 : 94, 12 : 88, and 25 : 75, respectively. For each condition, three distinct polymer sequences were prepared, with 10 chains per sequence, resulting in a total of 30 SBR chains placed on the CNF surface at a density of 0.98 g cm^{-3} at 298 K. After relaxation in the NVT ensemble at 500 K for 0.5 ns, a vacuum layer was added on top to complete the layered model. The final simulation box dimensions were 8.0 × 8.3 × 8.9 nm^3. MD simulations were subsequently performed for 2 ns at 298 K to investigate the interfacial structure, during which 200 data points were sampled at 10 ps intervals and used for the analysis.

3. Results and discussion

Before evaluating the SBR sheets kneaded with CNF, we first examined how the SFG spectra of SBR depend on the St content and how they are affected by the CNF addition. Well-defined SBR films with varying St contents were prepared in the laboratory *via* a solvent-casting method. Fig. 2(a) shows the SFG spectra in the C–H stretching region for solvent-cast SBR6, SBR12, and SBR25 films, with the spectra vertically offset for clarity. Based on the current measurement conditions, including the Fresnel coefficients and film thickness, the detected SFG signals were confirmed to originate predominantly from the film surface rather than from the substrate interface.

The prominent peak at 2905 cm^{-1} is attributed to the antisymmetric C–H stretching vibration of methylene groups (CH_2as) in Bd units[32] and the C–H stretching vibration of methyne (CH) groups in St units. Another peak at 2840 cm^{-1} is assigned to the symmetric C–H stretching vibration of methylene groups (CH_2s) from both St and Bd units.[32] A broad feature observed in the 2950 to 3015 cm^{-1} region corresponds to the C–H stretching vibration of methyne groups in CH═CH from 1,4-Bd units (2979 cm^{-1}) and the symmetric C–H stretching of vinyl methylene groups (═CH_2s) in 1,2-Bd units (2999 cm^{-1}).[53] A small peak at 3055 cm^{-1}, observed only in the SBR25 film, is assigned to the aromatic ν_2 mode.[54–56] These results indicate that both St and Bd segments are exposed at the air interface regardless of the St content, consistent with the random copolymer nature of the samples.

Fig. 2(b) shows the SFG spectra in the CH region for solvent-cast SBR6, SBR12, and SBR25 films with the addition of 1 wt% CNF. Clear signals were detected only for SBR25/CNF, whereas no distinct peaks appeared for SBR6/CNF and SBR12/CNF. The absence of signals in the latter two cases may be due to increased surface roughness upon CNF addition. This effect was particularly pronounced for these samples. Scattering of the incident light caused by the roughened surfaces was even visible to the naked eye. SFG measurements were conducted at multiple locations on each of three independently prepared samples, and consistent trends were confirmed across all measured positions. To assess the effect of surface roughness, solvent-cast SBR/CNF films were flattened before SFG measurements by pressing them with a Teflon sheet. This treatment markedly suppressed visible light scattering and reproduced the St content dependent increase in SFG intensity as discussed below, supporting the interpretation that surface roughness disturbed the measurements in the as-prepared films.

For SBR25/CNF, vibrational peaks corresponding to the ═CH_2s mode in 1,2-Bd units and the aromatic ν_2 mode were observed. Signals near the wavenumber of the 1,2-Bd peak also appeared in the spectrum of the neat CNF film (Fig. 2(c)), which exhibited prominent peaks at 2945 and 2968 cm^{-1}. These features in the SBR25/CNF spectrum are therefore likely to be at least partly attributable to CNF. The former peak can be assigned to the antisymmetric C–H stretching vibration of methylene groups in exocyclic CH_2OH groups (OCH_2as).[57] The latter is most likely due to CNF, as supported by the spectrum in Fig. 2(c). Although Kim *et al.* previously investigated the vibrational origin of this band using infrared spectroscopy, Raman spectroscopy, and DFT calculations, its assignment remains inconclusive.[58]

Under the present measurement conditions, SFG signals were observed exclusively for the SBR25/CNF film. In this sample, SBR/CNF interfaces were present not only at the film surface and the substrate interface but also within the bulk interior. We hypothesize that, for SBR25/CNF, the contribution from the buried interfaces differs markedly from that in SBR6/CNF and SBR12/CNF. Identifying which specific interface is responsible for the observed SFG signals will therefore be important.

The area of the buried interface between SBR and CNF within a film increases with film thickness. To examine how this affects the SFG response, measurements were taken on SBR25/CNF films with thicknesses of approximately 16, 33,

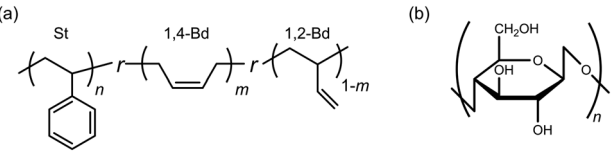

Fig. 1 Chemical structures of (a) SBR and (b) CNF.

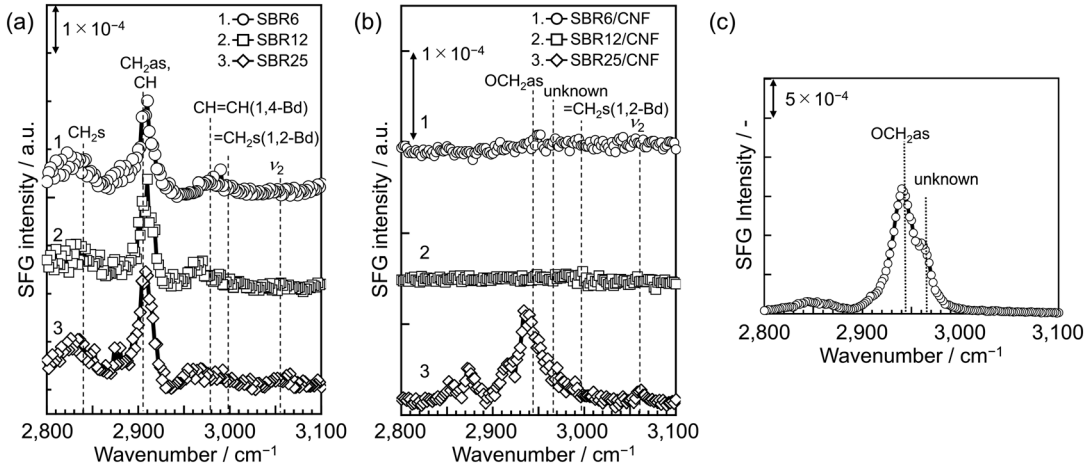

Fig. 2 SFG spectra collected with the ssp polarization combination for (a) solvent-cast SBR films with varying St contents, (b) solvent-cast SBR films containing 1 wt% CNF, and (c) a neat CNF film.

and 63 μm. Fig. 3(a) shows the SFG spectra in the CH stretching region for these films, collected under the ssp polarization combination and vertically offset for clarity. All spectra exhibit peaks at 2905 cm^{-1}, corresponding to the CH_2as mode in Bd units[32] and the CH mode in St units,[32] at 2945 cm^{-1}, attributed to the OCH_2as mode in CNF,[57] and at 3055 cm^{-1}, assigned to the ν_2 mode of phenyl rings in St units.[54–56] The peak at 2945 cm^{-1} appeared most intense and overlapped with an additional feature around 2968 cm^{-1}. Comparison with the SFG spectrum of the neat CNF film shown in Fig. 2(c) indicates that this spectral profile indeed reflects interfacial signals originating from the SBR/CNF interface, particularly those located within the bulk.

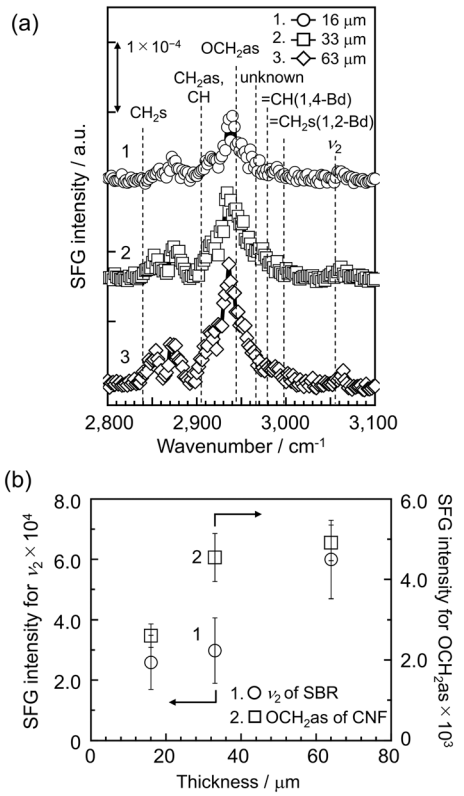

Fig. 3 (a) SFG spectra in the C–H stretching region for solvent-cast SBR25/CNF films with varying thicknesses, collected under the ssp polarization combination. Spectra are vertically offset for clarity. (b) Thickness dependence of the SFG signal intensities corresponding to the ν_2 mode of SBR and the OCH_2as mode of CNF, extracted from the spectra in panel (a).

Fig. 3(b) shows the film thickness dependence of SFG intensity for the ν_2 mode of phenyl rings of St moieties in SBR and the OCH_2as mode in CNF. Notably, the SFG intensity of the SBR25/CNF films increased with increasing thickness, in contrast to typical observations.[43,59,60] Generally, when excitation beams are incident from the film surface, the surface contribution to the SFG signal remains constant with thickness, whereas the substrate interface contribution decreases due to attenuation of the incident IR beam.

Consequently, the total SFG intensity typically decreases or becomes independent of thickness once the film exceeds the IR penetration depth.

The increase in SFG intensity observed here, contrary to the typical thickness-dependent decrease, points to major contributions from buried interfaces between the SBR matrix and CNF fillers. Similar behavior has been reported for polymer films containing crystallites, where inversion symmetry breaking at crystalline and amorphous interfaces generates SFG signals and their effective area increases with thickness, provided the excitation beams penetrate the film.[43] By analogy, the SFG signals observed here can be attributed to the buried SBR/CNF boundaries, reflecting the local orientation of functional groups at these internal interfaces. The eventual saturation of SFG intensity with thickness is likely due to the film exceeding the IR penetration depth, thereby limiting further signal generation.

If the aforementioned hypothesis is valid, SFG signals originating solely from internal SBR/CNF interfaces should be detectable under conditions that exclude contributions from both the air-facing surface and the substrate interface. This can be achieved by tilting the sample so that reflected

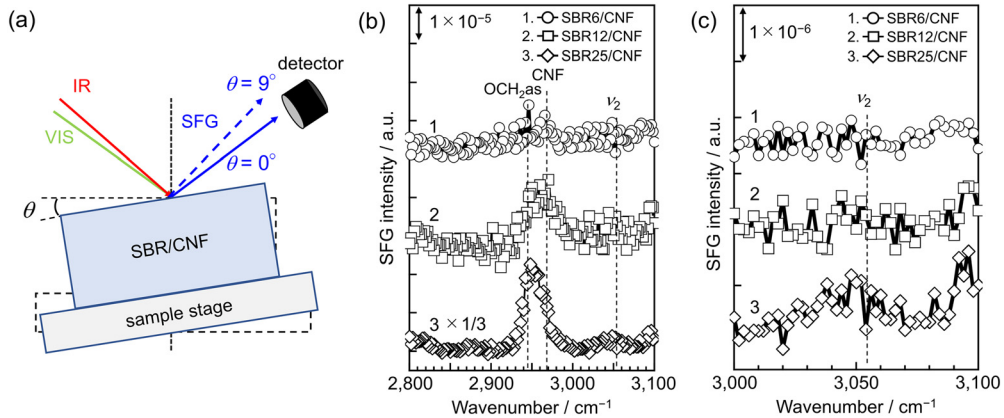

Fig. 4 (a) Schematic illustration of the experimental setup at θ = 0° and θ = 9°. (b) SFG spectra in the C–H region for SBR6/CNF, SBR12/CNF, and SBR25/CNF sheets obtained at θ = 9°, where surface and substrate interface contributions are suppressed. (c) Enlarged view of the aromatic C–H vibration region extracted from panel (b).

SFG signals from these external interfaces are directed away from the detector. Fig. 4(a) shows the experimental setup for both the standard (θ = 0°) and tilted (θ = 9°) configurations, where θ denotes the angle of the sample relative to the horizontal plane. In the standard configuration, the sample is positioned parallel to the optical table, allowing SFG signals from both the air facing surface and the substrate interface to be collected. In contrast, tilting the sample to θ = 9° deflects SFG signals from these external interfaces away from the detector, thereby isolating contributions from buried internal interfaces.

To verify this approach, a control experiment was conducted using a 200 nm-thick poly(methyl methacrylate) (PMMA) film, a polymer known to exhibit strong SFG signals, as a reference. Since the PMMA film contained no fillers, its SFG response was expected to originate solely from the surface and substrate interface. Fig. S1 shows the SFG spectra obtained from the PMMA film at θ = 0° and 9°. At θ = 0°, characteristic PMMA peaks were clearly observed. At θ = 9°, however, no SFG signals were detected, confirming that contributions from the external interfaces are eliminated under this tilted geometry.

SFG measurements were then taken to probe buried SBR/CNF interfaces in the kneaded composite sheets. Fig. 4(b) shows the SFG spectra in the C–H stretching region obtained at θ = 9° for the kneaded SBR6/CNF, SBR12/CNF, and SBR25/CNF sheets, and Fig. 4(c) provides an enlarged view of the 3000–3100 cm^{-1} region. Peaks attributable to CNF were observed at 2945 and 2960 cm^{-1} in all three samples. In addition, a distinct peak at 3055 cm^{-1}, assigned to the ν_2 mode of phenyl rings in St units, was detected exclusively in the kneaded SBR25/CNF sheet. The appearance of the ν_2 peak indicates that phenyl groups in SBR were oriented at the SBR/CNF interfaces. In contrast, this peak was absent in the kneaded SBR6/CNF and SBR12/CNF sheets, which may be due to a lack of orientational ordering of phenyl rings at the CNF interfaces, a low population of oriented phenyl rings, or a smaller effective interfacial area between SBR and CNF.

To further clarify the factors underlying the differences in SFG intensity, we examined the interfacial molecular structure from three perspectives: phenyl group orientation, the number density of phenyl groups determined by St content, and the extent of effective interfacial area in the composites. In principle, SFG spectroscopy enables estimation of the orientational angle of functional groups at interfaces in planer systems. However, this approach was not applicable here because CNF fillers were dispersed within the SBR matrix, resulting in spatially heterogeneous interfaces where a uniform orientational angle of phenyl groups cannot be defined. Thus, MD simulations were employed to discuss their local orientation. Fig. 5 shows the distribution of tilt angles (ϕ) of phenyl groups in SBR6, SBR12, and SBR25 at the CNF interface. The orientation angle is defined relative to the surface normal of the CNF interface (see Fig. S2 in the SI). For all SBR systems, the distributions peaked around 120°, indicating that phenyl rings preferentially adopt an orientation nearly parallel to the CNF surface. The similarity of these angular distributions across compositions suggests

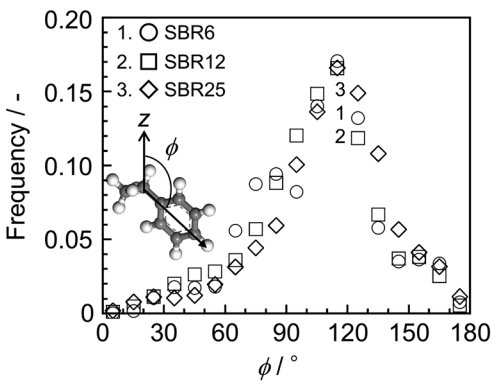

Fig. 5 Orientational angle distribution of phenyl groups in the St units at the SBR/CNF interface for SBR6, SBR12, and SBR25, obtained from MD simulations. The orientation angle is defined relative to the surface normal of the CNF interface.

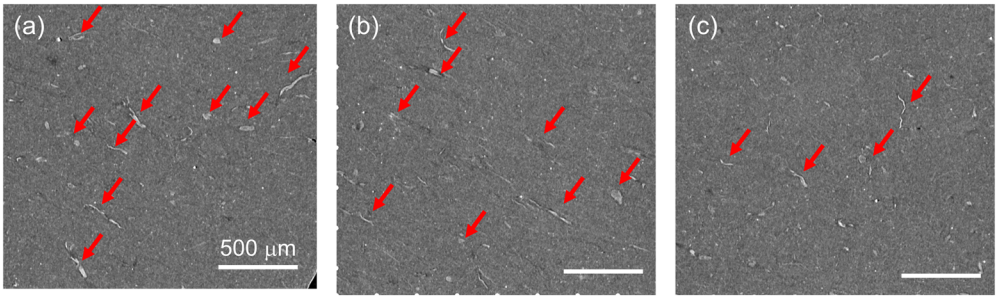

Fig. 6 X-ray CT images for (a) SBR6/CNF, (b) SBR12/CNF, and (c) SBR25/CNF sheets.

that the local phenyl group orientation at the CNF interface is largely independent of St content.

Next, we consider whether the number density of phenyl groups at the CNF interface increases with increasing St content in SBR, potentially leading to a corresponding increase in SFG intensity. Because SBR is a random copolymer of St and Bd, even if St units preferentially localize at the CNF interface through thermodynamic interactions, adjacent Bd units would likely still be present. This makes selective accumulation of phenyl groups at the interface unlikely. To assess this, we examined the SFG intensities of the SBR/CNF sheets. As shown in Fig. 4, no such trend was evident, particularly in the ν_2 mode of the phenyl rings, suggesting that the observed differences do not originate from variations in the interfacial number density of phenyl groups.

The difference in SFG intensity among the SBR6/CNF, SBR12/CNF, and SBR25/CNF composites cannot be explained by the orientation or number density of phenyl groups at the buried CNF interfaces, as discussed above. This conclusion is supported by MD simulations, which showed similar orientation distributions across all SBR compositions, and by the absence of a proportional increase in the ν_2 peak intensity with increasing St content. These findings suggest that the variation in SFG signal intensity among the samples is primarily attributable to differences in interfacial area.

If this hypothesis is correct, increasing the St content in SBR should enhance the dispersibility of CNF. To evaluate the dispersion state of CNF fillers, X-ray CT was used to directly visualize their distribution within the SBR matrix. Fig. 6 shows X-ray CT images of the kneaded SBR6/CNF, SBR12/CNF, and SBR25/CNF sheets. The scale bar corresponds to 500 μm. As indicated by the red arrows, CNF fibril-like aggregates (white) were observed in all images. However, the number of aggregates decreased markedly with increasing St content and became undetectable at this scale in SBR25/CNF, demonstrating that CNF dispersion improved with St content.

To further assess CNF dispersion, the transmittance of visible light was measured. As shown in Fig. S3, despite all sheets containing the same CNF content, the SBR25/CNF composite exhibited the highest transmittance, consistent with the X-ray CT observations.

To investigate the origin of the differences in CNF dispersion, the surface free energy (γ) of the SBRs was evaluated using the Owens–Wendt method, based on contact angle measurements with water and diiodomethane as probe liquids.[61] Fig. 7 shows the dependence of γ on the St fraction in the SBR samples. For reference, γ was also measured for PS (M_n = 180k, M_w/M_n = 1.05), corresponding to 100% St content (SBR100). The γ of the SBRs increased with St content, consistent with the relatively low γ of the rubbery Bd units. The dashed line in Fig. 7 represents the γ of a CNF sheet prepared by pressing a CNF mat obtained *via* suction filtration of an aqueous CNF dispersion, measured using the same method. This value agreed well with reported γ values for cellulose derived from cotton.[62] Among the SBR samples examined, SBR25 exhibited the smallest γ difference relative to cellulose, indicating the most favorable condition for CNF dispersion. Consequently, the interfacial area in the composite is maximized, leading to the highest SFG signal intensity. These results suggest that differences in filler dispersion may also influence the mechanical properties. Although improved CNF dispersion in the SBR25/CNF system is expected to enhance the reinforcing effect, variation in the St content also directly alters intrinsic matrix properties such as T_g and elastic modulus. Therefore, establishing a clear structure–property relationship that incorporates interfacial effects will require further systematic studies with independently controlled composition and structure.

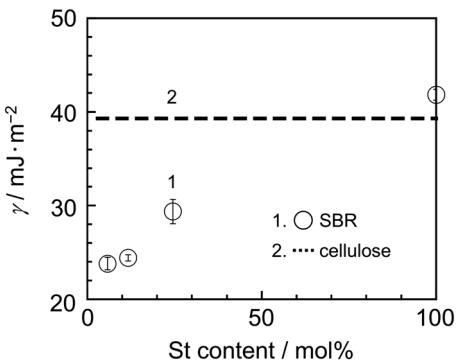

Fig. 7 Surface free energy of SBRs with varying St fractions and of CNF (dashed line), determined from contact angle measurements following the Owens–Wendt method.

4. Conclusions

The interfacial aggregation states of SBR in CNF-reinforced composites were systematically investigated using SFG vibrational spectroscopy in combination with MD simulations. Initially, SFG spectra of SBR/CNF composites were compared with those of corresponding neat SBR films with varying St content, revealing distinct spectral features in the composites that were absent in the neat films. SFG spectra obtained from SBR/CNF samples with varying thicknesses confirmed that the observed signals originated not only from the surface but also from internal SBR/CNF interfaces. To selectively probe these buried interfaces, a tilted sample geometry was introduced, under which vibrational signals were detected exclusively for the SBR25/CNF composite, indicating that phenyl groups in St units were oriented at the CNF interface. This molecular-level orientation was not evident in the SBR6 or SBR12 composite films. The enhancement in SFG intensity was attributed not to differences in local orientation or phenyl group density but rather to an increased effective interfacial area resulting from improved CNF dispersion. This interpretation was corroborated by X-ray CT scanning, visible light transmittance measurements, and surface free energy analysis, which collectively demonstrated favorable interfacial energy matching between SBR25 and CNF. Overall, these findings demonstrate that tuning the chemical composition of the polymer matrix enables control over filler dispersion and interfacial molecular organization, offering molecular-level guidelines for the rational design of high-performance, bio-based polymer composites and advancing the development of sustainable materials technologies.

Author contributions

Tatsuki Abe: data curation, formal analysis, methodology, investigation, writing – original draft. Ryosuke Ozawa: resources, data curation. Tomofumi Maekawa: resources, data curation. Yuta Tsuji: data curation, formal analysis. Satoru Yamamoto: data curation, formal analysis, writing – original draft. Keiji Tanaka: project administration, conceptualization, funding acquisition, resources, methodology, writing – review & editing, supervision. All authors discussed the results and contributed to the final manuscript.

Conflicts of interest

The authors have no conflicts to disclose.

Data availability

The data supporting this article will be available upon request at https://www.cstf.kyushu-u.ac.jp/~tanaka-lab/english/.

Supplementary information (SI) available: SFG spectra for PMMA thin film at sample installation angle (θ) (a) 0° and (b) 9°. Phenyl group orientation analysis by MD simulation. The visible wavelength dependence of transmittance for SBR/CNF sheets with various St contents. See DOI: https://doi.org/10.1039/d6lf00054a.

Acknowledgements

This work was supported by JSPS KAKENHI for Scientific Research (B) (No. JP26K01559) to KT and for Early Career Scientists (No. JP25K18073) to TA. We are also thankful for the support from the JST-Mirai Program (JPMJMI18A2) (KT).

Notes and references

1 B. Erman and J. E. Mark, *Structures and Properties of Rubberlike Networks*, Oxford University Press, New York, 2nd edn, 1997.
2 *Rubber Technology*, ed. M. Morton, Springer, Dordrecht, 1999.
3 S. Wolff, *Rubber Chem. Technol.*, 1996, **69**, 325–346.
4 G. Kraus, *Rubber Chem. Technol.*, 1965, **38**, 1070–1114.
5 S. Kaufman, W. P. Slichter and D. D. Davis, *J. Polym. Sci., Part A:Polym. Chem.*, 1971, **9**, 829–842.
6 T. Nishi, *J. Polym. Sci., Polym. Phys. Ed.*, 1974, **12**, 685–700.
7 Y. Shui, L. Huang, C. Wei, G. Sun, J. Chen, A. Lu, L. Sun and D. Liu, *Compos. Sci. Technol.*, 2021, **215**, 109024.
8 H. Schneider, M. Roos, Y. Golitsyn, K. Steiner and K. Saalwächter, *Macromol. Rapid Commun.*, 2021, **42**, 2100061.
9 K. U. Kirst, F. Kremer and V. M. Litvinov, *Macromolecules*, 1993, **26**, 975–980.
10 J. G. Meier, J. W. Mani and M. Klüppel, *Phys. Rev. B: Condens. Matter Mater. Phys.*, 2007, **75**, 054202.
11 M. A. Sattar and A. Patnaik, *ACS Omega*, 2020, **5**, 21191–21202.
12 A.-C. Genix, V. Bocharova, B. Carroll, P. Dieudonné-George, E. Chauveau, A. P. Sokolov and J. Oberdisse, *ACS Appl. Mater. Interfaces*, 2023, **15**, 7496–7510.
13 J. C. Kenny, V. J. McBrierty, Z. Rigbi and D. C. Douglass, *Macromolecules*, 1991, **24**, 436–443.
14 D. Fragiadakis, L. Bokobza and P. Pissis, *Polymer*, 2011, **52**, 3175–3182.
15 D. Luo, H. Wu, H. Li, W. Zhang, L. Zhang and Y. Gao, *Polymer*, 2022, **246**, 124750.
16 N. K. Weise, B. P. Mason, C. M. Roland and P. H. Mott, *Rubber Chem. Technol.*, 2024, **97**, 523–532.
17 S. Kohjiya, A. Kato and Y. Ikeda, *Prog. Polym. Sci.*, 2008, **33**, 979–997.
18 N. Torbati-Fard, S. M. Hosseini and M. Razzaghi-Kashani, *Polym. J.*, 2020, **52**, 1223–1234.
19 D. Dhara, M. A. Rahman, E. Ruzicka, A. Karekar, D. Vlassopoulos, K. Saalwächter, B. Benicewicz and S. K. Kumar, *Macromolecules*, 2024, **57**, 1448–1460.
20 T. Koga, X. Wang, Z. Huang, Y. Bajaj, M. Endoh, J.-M. Y. Carrillo, B. G. Sumpter, T. Masui, H. Kishimoto, T. Taniguchi, Z. H. Lin, A. E. Ribbe, H. Zhang, R. Li, L.

Wiegart, N. C. Osti, T. Yamada, L. Porcar, B. Farago, J. Allgaier, M. Kruteva, M. Monkenbusch, M. Richter, D. Nagao and M. How, *Macromolecules*, 2025, **58**, 9182–9198.
21 S. S. Sternstein and A. J. Zhu, *Macromolecules*, 2002, **35**, 7262–7273.
22 A. J. Zhu and S. S. Sternstein, *Compos. Sci. Technol.*, 2003, **63**, 1113–1126.
23 Q. Chen, S. Gong, J. Moll, D. Zhao, S. K. Kumar and R. H. Colby, *ACS Macro Lett.*, 2015, **4**, 398–402.
24 Y. Wang, M. Sun, H. Zhang, Y. Lu, W. You, F. Bian and W. Yu, *Macromolecules*, 2023, **56**, 934–946.
25 C. Marzolin, P. Auroy, M. Deruelle, J. P. Folkers, L. Léger and A. Menelle, *Macromolecules*, 2001, **34**, 8694–8700.
26 S. Shimomura, M. Inutsuka, N. L. Yamada and K. Tanaka, *Polymer*, 2016, **105**, 526–531.
27 S. Z. Bhutia, S. Chandran, S. K. Sukumaran and D. K. Satapathy, *Macromolecules*, 2025, **58**, 3564–3577.
28 S. D. Kim and J. M. Torkelson, *Macromolecules*, 2002, **35**, 5943–5952.
29 H. K. Nguyen, A. Konomi, S. Sugimoto, M. Inutsuka, D. Kawaguchi and K. Tanaka, *Macromol. Chem. Phys.*, 2018, **219**, 1700329.
30 H. K. Nguyen, S. Sugimoto, A. Konomi, M. Inutsuka, D. Kawaguchi and K. Tanaka, *ACS Macro Lett.*, 2019, **8**, 1006–1011.
31 S. Sugimoto, M. Inutsuka, D. Kawaguchi and K. Tanaka, *ACS Macro Lett.*, 2018, **7**, 85–89.
32 B. Zuo, M. Inutsuka, D. Kawaguchi, X. P. Wang and K. Tanaka, *Macromolecules*, 2018, **51**, 2180–2186.
33 Z. Chen, Y. R. Shen and G. A. Somorjai, *Annu. Rev. Phys. Chem.*, 2002, **53**, 437–465.
34 Y. Oda, A. Horinouchi, D. Kawaguchi, H. Matsuno, S. Kanaoka, S. Aoshima and K. Tanaka, *Langmuir*, 2014, **30**, 1215–1219.
35 M. Inutsuka, A. Horinouchi and K. Tanaka, *ACS Macro Lett.*, 2015, **4**, 1174–1178.
36 H. S. Varol, M. A. Sánchez, H. Lu, J. E. Baio, M. Malm, N. Encinas, M. R. B. Mermet Guyennet, N. Martzel, D. Bonn, M. Bonn, T. Weidner, E. H. G. Backus and S. H. Parekh, *Macromolecules*, 2015, **48**, 7929–7937.
37 X. Lu, C. Zhang, N. Ulrich, M. Xiao, Y.-H. Ma and Z. Chen, *Anal. Chem.*, 2017, **89**, 466–489.
38 T. Lin, Y. Wu, E. Santos, X. Chen, J. Kelleher Ferguson, C. Tucker, D. Ahn, C. Mohler and Z. Chen, *Langmuir*, 2022, **38**, 2590–2600.
39 K. Uchida, K. Mita, S. Yamamoto and K. Tanaka, *Polym. J.*, 2023, **55**, 683–690.
40 T. Abe, S. Yamamoto and K. Tanaka, *Polym. Chem.*, 2024, **15**, 4425–4432.
41 J. Duan, C. Ding, J. Li, A. Hou, S. Zhang, H. Liu, W. Gan and R. Zhang, *Appl. Surf. Sci.*, 2025, **714**, 164464.
42 Y. Hu, B. Dai, Z. Xu, H. Chen and X. Lu, *Colloids Surf., A*, 2025, **714**, 164464.
43 D. Kawaguchi, K. Yamamoto, T. Abe, N. Jiang, T. Koga, S. Yamamoto and K. Tanaka, *Phys. Chem. Chem. Phys.*, 2021, **23**, 23466–23472.
44 T. Abe, H. Shimada, T. Hoshino, D. Kawaguchi and K. Tanaka, *Polym. J.*, 2022, **54**, 679–685.
45 J. Lee, J. Ryu, J. Choi, I. Chae and S. H. Kim, *Annu. Rev. Phys. Chem.*, 2025, **76**, 405–430.
46 C. Miao and W. Y. Hamad, *Cellulose*, 2013, **20**, 2221–2262.
47 H. Soeta, S. Fujisawa, T. Saito, L. Berglund and A. Isogai, *ACS Appl. Mater. Interfaces*, 2015, **7**, 11041–11046.
48 M. Ghasemlou, F. Daver, E. P. Ivanova, Y. Habibi and B. Adhikari, *Prog. Polym. Sci.*, 2021, **119**, 101418.
49 H. Gou, W. Fang, J. Zhu, H. Wang, Y. Ma and H. Fan, *ACS Appl. Polym. Mater.*, 2025, **7**, 3752–3763.
50 A. N. T. Ngoc, N. V. Trung, M. V. Tue, T. T. Huy, Q. N. Thi, H. T. Van, S. Morishita, T. H. Nguyen, H. Ajiro and T. T. Thi, *Polym. J.*, 2025, **57**, 527–538.
51 Y. Hata, *Polym. J.*, 2026, **57**, 31–41.
52 K. Tashiro and M. Gakhutishvili, *Polymer*, 2019, **171**, 140–148.
53 Y. Fang, B. Li, J. Yu, J. Zhou, X. Xu, W. Shao and X. Lu, *Surf. Sci.*, 2013, **615**, 26–32.
54 K. S. Gautam, A. D. Schwab, A. Dhinojwala, D. Zhang, S. M. Dougal and M. S. Yeganeh, *Phys. Rev. Lett.*, 2000, **85**, 3854–3857.
55 G. P. Harp, H. Rangwalla, M. S. Yeganeh and A. Dhinojwala, *J. Am. Chem. Soc.*, 2003, **125**, 11283–11290.
56 A. D. Curtis, A. R. Calchera, M. C. Asplund and J. E. Patterson, *Vib. Spectrosc.*, 2013, **68**, 71–81.
57 A. L. Barnette, L. C. Bradley, B. D. Veres, E. P. Schreiner, Y. B. Park, J. Park, S. Park and S. H. Kim, *Biomacromolecules*, 2011, **12**, 2434–2439.
58 C. M. Lee, N. M. A. Mohamed, H. D. Watts, J. D. Kubicki and S. H. Kim, *J. Phys. Chem. B*, 2013, **117**, 6681–6692.
59 Y. Tateishi, N. Kai, H. Noguchi, K. Uosaki, T. Nagamura and K. Tanaka, *Polym. Chem.*, 2010, **1**, 303–311.
60 T. Nishida, C. M. Johnson, J. Holman, M. Osawa, P. B. Davies and S. Ye, *Phys. Rev. Lett.*, 2006, **96**, 077402.
61 D. K. Owens and R. C. Wendt, *J. Appl. Polym. Sci.*, 1969, **13**, 1741–1747.
62 P. Luner and M. Sandell, *J. Polym. Sci., Part C*, 1969, **28**, 115–142.